Constraints and performance trade-offs in Auger-suppressed HgCdTe focal plane arrays

Constraints and performance trade-offs in Auger-suppressed HgCdTe focal plane arrays

MARCO VALLONE,[1,*] MICHELE GOANO,[1,2] FRANCESCO BERTAZZI,[1,2] GIOVANNI GHIONE,[1] STEFAN HANNA,[3] DETLEF EICH,[3] ALEXANDER SIECK,[3] AND HEINRICH FIGGEMEIER[3]

[1] *Politecnico di Torino, Dipartimento di Elettronica e Telecomunicazioni, Corso Duca degli Abruzzi 24, 10129 Torino, Italy*
[2] *IEIIT-CNR, corso Duca degli Abruzzi 24, 10129 Torino, Italy*
[3] *AIM Infrarot-Module GmbH, Theresienstraße 2, D-74072 Heilbronn, Germany*
[*] *marco.vallone@polito.it*

Abstract: Majority carrier depletion has been proposed as a method to suppress the dark current originating from quasi-neutral regions in HgCdTe infrared focal plane array detectors. However, a very low doping level is usually required for the absorber layer, a task quite difficult to achieve in realizations. In order to address this point, we performed combined electromagnetic and electric simulations of a planar 5×5 pixels miniarray with 5 μm-wide square pixels, assessing the effect of the absorber thickness, its doping level in the interval $N_D = [10^{14}, 10^{15}]\,\mathrm{cm}^{-3}$, and temperature in the interval 140 K – 230 K, both in dark and under illumination. Looking for a trade-off, we found that the path towards high-temperature operation has quite stringent requirements on the residual doping, whereas a reduction of the absorber thickness helps only moderately to reduce the dark current. Under illumination, inter-pixel crosstalk is only slightly cut down by a decrease of temperature or absorber doping in the considered intervals, whereas it gets more effectively reduced by thinning the absorber.

1. Introduction

Among the several possible choices for the realization of large format, state-of-the-art, infrared (IR) photodetectors based on two-dimensional focal plane arrays (FPAs) of pixels, the II-VI alloy HgCdTe offers outstanding performances and great versatility [1–5]. However, particular technical and design adjustments are needed, in order to reduce the dark current without employing expensive and heavy cryogenic cooling systems [6–8]. In view of obtaining room-temperature operation, different solutions for High Operating Temperature (HOT) detectors [9–14] have been developed, e.g. considering *n*B*n* barrier detectors [15–17] or with fully-depleted double-layer planar heterostructures [18] with appropriate composition and doping profiles. The latter approach, in particular, is potentially suitable to suppresses the Auger carrier generation [8, 18–20], and when combined with the adoption of $Hg_{1-x}Cd_xTe$ absorbers with fine-tuned compositional grading, it has recently been indicated as a method to optimize the quantum efficiency (QE) [21].

In advanced IR imaging systems conceived for civilian and military applications, the spatial resolution greatly depends on the density of pixels per unit area [1–3, 6, 22–26]. Very small values for the pixel pitch P are often considered in order to obtain diffraction-limited optical systems fulfilling the Nyquist criterion [25, 27–30], namely $\approx 3\,\mu$m for the mid-wavelength IR band (MWIR, wavelength $\lambda \in [3, 5]\,\mu$m) and $\approx 5\,\mu$m for the long-wavelength IR band (LWIR, $\lambda \in [8, 14]\,\mu$m). In these conditions, the inter-pixel crosstalk [24] can become a limiting factor especially when planar structures are considered, and the importance of keeping it as low as possible cannot be neglected (in the present work, with *inter-pixel crosstalk* we mean the electrical response of a FPA pixel when an IR beam illuminates another pixel of the array, excluding any contribution from the read-out integrated circuit).

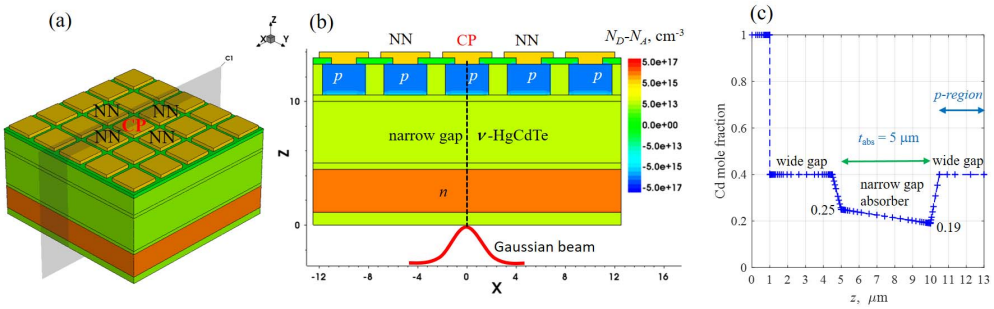

Fig. 1. (a) The 3D miniarray under investigation. CP and NN indicate respectively the central (CP) and the nearest neighboring (NN) pixels. (b) The doping distribution $N_D - N_A$ shown in a two dimensional (2D) cutplane at center pixel, with a sketch of the illumination as a narrow Gaussian beam focused on the central pixel from below. (c) The $Hg_{1-x}Cd_xTe$ composition profile x along the vertical z-cutline at miniarray center shown in (b), with an indication of the p-doped region extension.

In a recent work [31] based on combined electromagnetic and electrical simulations, we assessed the role of majority carrier depletion as a method suitable for cutting down the diffusive inter-pixel crosstalk due to lateral carrier diffusion in planar FPAs operated in reverse bias, besides obtaining a substantial reduction of dark current. However, this goal was obtained considering a very low value for doping concentration N_D in the HgCdTe absorber ($N_D = 10^{14}$ cm^{-3}) and an operating temperature $T = 140$ K. Still considering the same detector [31] and extending the simulation plan up to $T = 230$ K, the present work assesses how large is the expected increase of dark current when the initial stringent requirement on N_D is relaxed, also investigating whether it is possible to compensate the effect with a reduction of absorber thickness t_{abs}. In addition, by numerical simulations under illumination, we describe how the inter-pixel crosstalk and quantum efficiency are affected by T, N_D, t_{abs}, and reverse bias V_{abs}. Therefore, after a short description of the detector in Section 2 and a review of the computational methods in Section 3, the obtained results are presented and discussed in Section 4. Finally, Section 5 summarizes the main outcomes of this study.

2. Detector structure and illumination conditions

In Ref. [31] we considered a small modification of an epitaxial structure described in the literature [21], known to be able to cut down the dark current by suppressing Auger generation via detector majority carriers depletion. This choice was motivated by our intention to show that majority carrier depletion is also helpful in decreasing the diffusive inter-pixel crosstalk.

Fig. 1 shows the photodetector structure, with the definitions of the central (CP) and the nearest neighboring (NN) pixels. Above a CdTe substrate, a wide-bandgap n-$Hg_{0.6}Cd_{0.4}Te$ layer, doped with donor concentration $N_D = 5\times10^{17}$ cm^{-3}, is followed by a low donor-doped, narrow-bandgap HgCdTe absorber layer, and by another wide-bandgap $Hg_{0.6}Cd_{0.4}Te$ layer above, with the same low donor concentration. Regarding the absorber layer thickness t_{abs}, we considered two variants: the original value employed in Ref. [31], $t_{abs} = 5\,\mu$m (variant A), and a thinner variant B with $t_{abs} = 2.5\,\mu$m. As anticipated in Section 1, for both variants we explored the effect of absorber donor doping, varying its concentration in the interval $N_D \in [10^{14}, 10^{15}]$ cm^{-3}, avoiding to investigate more challenging values $N_D < 10^{14}$ cm^{-3} , whose achievement is possible although difficult [21, 32] (in Ref. [31] the value chosen for N_D was 10^{14} cm^{-3}).

Considering this heterostructure, a planar 5×5 miniarray with 5 μm-wide square pixels was defined by simulating an ion implantation, yielding a p-n junction at a depth of $\approx 2.5\,\mu$m from

the bias contact. The absorber layer was given a graded composition, varying the Cd mole fraction from $x = 0.25$ to $x = 0.19$, from its lower to its upper interface. Even for low reverse bias, the quasi-electrical field ensuing from the compositional grading helps in sweeping-out the photogenerated minority carriers (holes) from the low donor-doped absorber, before they diffuse laterally contributing to crosstalk [33]. The bias contacts were connected to the p-doped regions through a square metallic layer partly extending over a $0.3\,\mu$m thick CdTe passivation layer that covers the upper face of the FPA. The HgCdTe properties were described taking into account their composition, doping, and temperature dependence according to the models reported in Ref. [29]. The Shockley-Read-Hall (SRH) recombination processes were modeled as in Ref. [34] considering a lifetime around $100\,\mu$s, neglecting instead trap-assisted or band-to-band tunneling processes [35–37]. Fermi-Dirac statistics and incomplete dopant ionization were taken into account, with activation energies for HgCdTe alloys estimated according to [38, 39].

The detector was simulated in dark and under illumination, considering for the latter case a narrow Gaussian beam illuminating the array from below, with the beam axis orthogonal to the detector horizontal plane xy, centered on the miniarray CP and focused on the illuminated face. The beam power flux profile is $\Phi(r) = \Phi_0 \exp\left(-2r^2/w_0^2\right)$, where Φ_0 is the optical power flux along the beam axis, r is the radial distance from the beam axis and $w_0 = 2.5\,\mu$m is the beam waist radius. It must be noticed that $\Phi(r)$ never goes to zero, hence the beam tail partially illuminates also the CP neighboring pixels.

3. Modeling method

The detector performace was investigated by combined electromagnetic (optical) and electric three-dimensional (3D) simulations performed employing a commercial numerical simulator by Synopsys [40], composed by a TCAD section to design the detector, an ElectroMagnetic Wave (EMW) solver, and an electron transport solver (SDEVICE), here employed in the drift-diffusion approximation. The EMW section was employed to obtain the solution of the electromagnetic problem under monochromatic illumination, which in turn provides the absorbed photon density A_{opt} (number of absorbed photons per unit volume and time) as the divergence of the time-averaged Poynting vector $\langle\vec{S}\rangle$ [41–44]

$$A_{\mathrm{opt}}(\lambda_n) = -\frac{\vec{\nabla}\cdot\langle\vec{S}(\lambda_n)\rangle}{hc/\lambda_n}. \tag{1}$$

Here h is the Planck constant, c is the light velocity in vacuum, and the material complex refractive index is included in $\vec{S}$ through Maxwell equations as shown e.g. in Ref. [29], Eqs. (8-10)). The optical generation rate distribution G_{opt} into the FPA due to interband optical absorption is given by $G_{\mathrm{opt}}(\lambda_n) = \eta A_{\mathrm{opt}}(\lambda_n)$, where the quantum yield η, defined as the fraction of absorbed photons which are converted to photogenerated electron-hole pairs, was assumed to be unitary.

For all the considered wavelengths $\lambda_n \in [2, 12]\,\mu$m of the illuminating IR radiation, the absorber and the transition regions compositional grading profiles were discretized to staircases of $N = 30$ sublayers with uniform complex refractive index $n_r + i\kappa$, evaluated according to each sublayer $Hg_{1-x}Cd_xTe$ composition ([29], Table I), as described in detail in Ref. [45]. Since a fine λ-sampling is important to describe and keep into account the rich resonance-like phenomenology especially around the cutoff-wavelength [29, 45], the λ interval was sampled considering 84 distinct λ-points: this implies that 84 distinct electromagnetic simulations in order to explore all the considered IR spectrum with enough detail.

The computational box includes air layers located above and below the miniarray, and the optical boundary conditions (BC) along all the sides of the box are absorbing (this is obtained with convolutional perfectly matching layers [46]). With this approach, the EMW block was able to solve the electromagnetic problem by a full-wave approach, according to the Finite Differences Time Domain (FDTD) method and discretizing the miniarray into a Yee grid of $\approx 3.4 \times 10^6$

elements [47, 48].

The electrical problem was solved within the drift-diffusion approximation, as outlined e.g. in Ref. [29, 49–51]. Electric contacts were treated as Ohmic with zero resistance, where charge neutrality and equilibrium were assumed. Ideal Neumann BCs were applied to the outer boundaries of the array, and the drift-diffusion equations were solved by the Finite Box (FB) method, setting the desired temperature and reverse-biasing the detector from 0V to −0.5 V, applying the same voltage to all the pixels. Electrical simulations were obtained considering Auger and SRH as generation-recombination (GR) processes, neglecting instead radiative processes. Extensive discussion about this important point can be found in Ref. [52] and references therein. At the moderate reverse bias considered in the present work, the band-to-band, trap-assisted tunneling and impact ionization may be safely neglected [34–36].

The electrical problem was first solved in dark, obtaining the dark current $I_{\mathrm{dark},i}$, expected to be very similar for all the pixels (the subscript i marks the i-th pixel). When the FPA is illuminated, $G_{\mathrm{opt}}(\lambda_n)$ enters as a source term in the current continuity equations, providing the current $I_i(\lambda_n)$ collected by all the pixels, from which the photocurrent follows as $I_{ph,i}(\lambda_n) = I_i(\lambda_n) - I_{\mathrm{dark},i}$. The external quantum efficiency is defined as

$$\mathrm{QE}_i(\lambda_n) = \frac{I_{ph,i}(\lambda_n)}{qN_{\mathrm{phot},i}(\lambda_n)}, \tag{2}$$

where q is the elementary charge and $N_{\mathrm{phot},i}$ is the photon flux impinging the i-th pixel illuminated face. To this end, the detector in Fig. 1 was discretized into $\approx 0.95 \times 10^6$ elements with a meshing tool which generates a denser grid in regions where gradients of current density, electric field, free charge density and material composition are present.

The ratio C_i between the photocurrent collected by the electrical contacts of the i-th pixel and of the CP,

$$C_i(\lambda_n) = \frac{I_{ph,i}(\lambda_n)}{I_{ph,\mathrm{CP}}(\lambda_n)}, \tag{3}$$

can be regarded as a possible definition of the *total* inter-pixel crosstalk. Considering the NNs, $C_{\mathrm{NNs}}(\lambda_n)$ depends on carriers photogenerated in the CP diffusing to the neighboring ones (yielding a *diffusive* crosstalk, $\mathcal{D}_{\mathrm{NNs}}(\lambda_n)$), but it also depends on carriers directly photogenerated in the NNs by the illuminating Gaussian beam tail [29] (*optical* crosstalk). The latter can be defined as

$$O_{\mathrm{NNs}}(\lambda_n) = \frac{\int_{V_{\mathrm{NNs}}} G_{\mathrm{opt}}(x,y,z;\lambda_n)\,dx\,dy\,dz}{\int_{V_{\mathrm{CP}}} G_{\mathrm{opt}}(x,y,z;\lambda_n)\,dx\,dy\,dz}, \tag{4}$$

where $V_{\mathrm{CP,NNs}}$ is the CP (NNs) volume. Regarding the diffusive inter-pixel crosstalk $\mathcal{D}_{\mathrm{NNs}}$, following the approach described in a previous work [53], it can be approximated as

$$\mathcal{D}_{\mathrm{NNs}} \approx C_{\mathrm{NNs}} - O_{\mathrm{NNs}}, \tag{5}$$

and the figures of merit I_{dark}, $\mathrm{QE}_{\mathrm{CP}}(\lambda_n)$, and $\mathcal{D}_{\mathrm{NNs}}(\lambda_n)$ provide together an evaluation of the expected detector performance as function of several geometrical, compositional and illumination parameters.

4. Results and discussion

First we present the results of simulations obtained in dark, for variants A and B, discussing the effect of absorber thickness, doping concentration, and temperature. Then, we discuss the effect of these quantities on the detector performance under illumination, simulating its optical and electrical response when a narrow Gaussian beam illuminates the miniarray as described in Section 2.

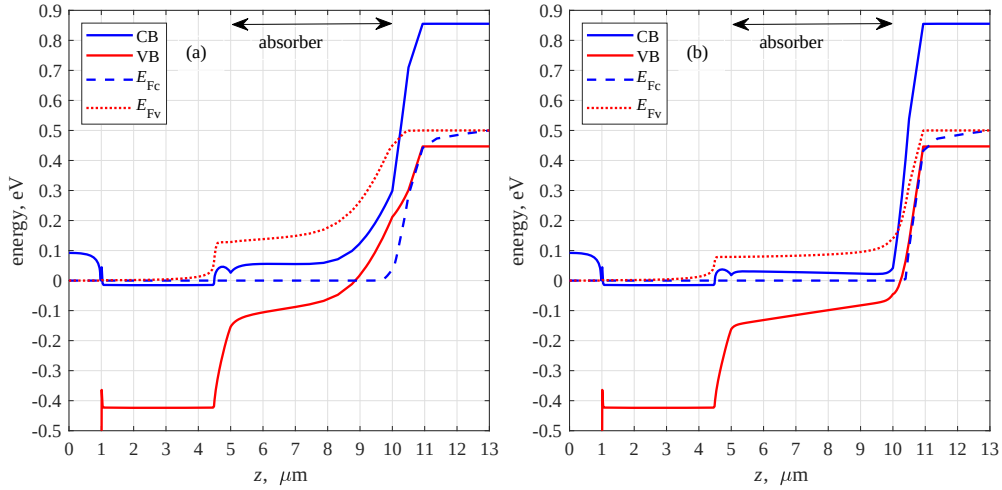

Fig. 2. Variant A, $T = 140\,\mathrm{K}$, $V_{\mathrm{bias}} = -0.5\,\mathrm{V}$: band diagrams in reverse bias along a vertical z-line at miniarray center, calculated with (a) $N_{\mathrm{D}} = 10^{14}\ \mathrm{cm}^{-3}$ and (b) $N_{\mathrm{D}} = 10^{15}\ \mathrm{cm}^{-3}$. The narrow bandgap absorber is in $5 \le z \le 10$.

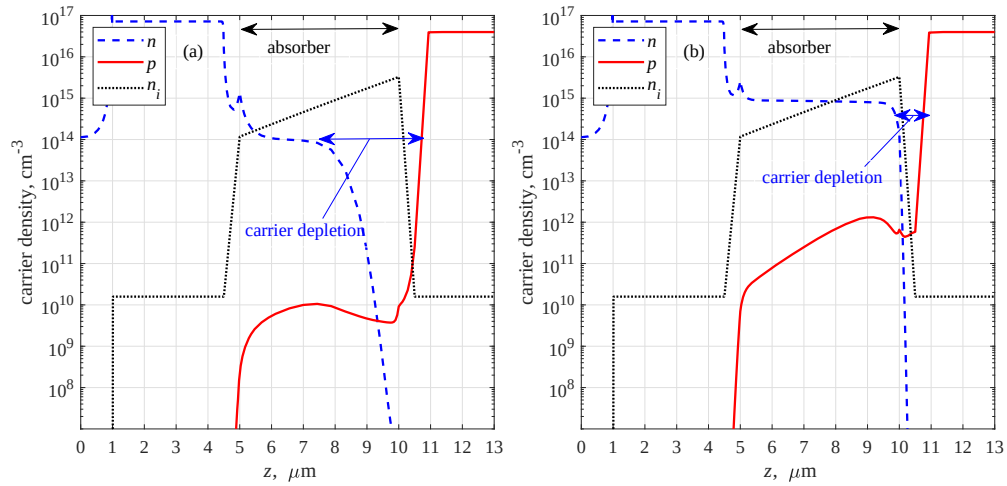

Fig. 3. Variant A, $T = 140\,\mathrm{K}$, $V_{\mathrm{bias}} = -0.5\,\mathrm{V}$: electron ($n$), hole ($p$) and intrinsic density (n_i) along a vertical z-line at miniarray center, calculated for (a) $N_{\mathrm{D}} = 10^{14}\ \mathrm{cm}^{-3}$ and (b) $N_{\mathrm{D}} = 10^{15}\ \mathrm{cm}^{-3}$. In panel (b), the absorber region depleted from majority carriers (electrons) in practice disappears.

4.1. Simulations in dark

Considering the variant A (characterized by thicker absorber) as a reference, we begin the analysis comparing the detector characteristics in dark for $N_D = 10^{14}\ \mathrm{cm}^{-3}$ and $N_D = 10^{15}\ \mathrm{cm}^{-3}$ at the operating temperature $T = 140\,\mathrm{K}$, driving the detector from equilibrium to reverse bias ($V_{\mathrm{bias}} = -0.5\,\mathrm{V}$ applied simultaneously to the bias contacts).

Fig. 2 shows the band diagram in reverse bias along a vertical z-cutline at miniarray center. When N_D increases, bands become flatter in a large part of the absorber, and quite steeper in a $1\,\mu\mathrm{m}$ thick region close to the bias contact, above the absorber. For $N_{\mathrm{D}} = 10^{14}\ \mathrm{cm}^{-3}$, the moderate steepness of the conduction and valence band (CB, VB) is sufficient to efficiently

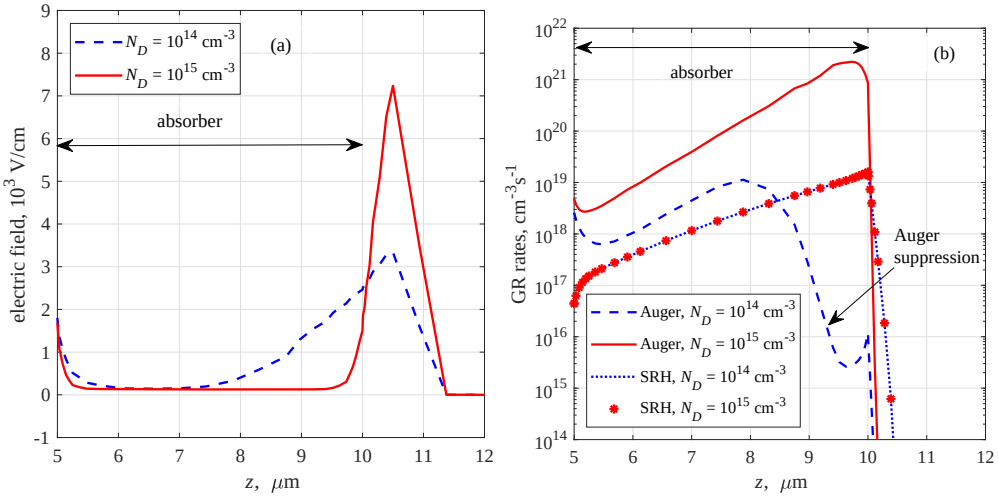

Fig. 4. Variant A, $T = 140\,\mathrm{K}$, $V_{\mathrm{bias}} = -0.5\,\mathrm{V}$: (a) magnitude of the electric field, and (b) Auger and SRH generation rates along a vertical z-line at miniarray center, calculated for $N_{\mathrm{D}} = 10^{14}\ \mathrm{cm}^{-3}$ and $N_{\mathrm{D}} = 10^{15}\ \mathrm{cm}^{-3}$. For $N_{\mathrm{D}} = 1 \times 10^{14}\ \mathrm{cm}^{-3}$, the suppression of Auger generation is well evident (blue dashed line in panel (b)), whereas for $N_{\mathrm{D}} = 1 \times 10^{15}\ \mathrm{cm}^{-3}$ the effect in practice disappears (red solid line).

deplete it from majority carriers at least in its upper part, as visible in Fig. 3(a). This mechanism gets substantially reduced as soon as the donor doping increases to $N_{\mathrm{D}} = 10^{15}\ \mathrm{cm}^{-3}$, Fig. 3(b): carrier depletion is limited to a narrow region $10 \lessapprox z \lessapprox 10.5$ outside the absorber, that in practice is not depleted. This happens because the electric field is very close to zero throughout the absorber, as visible in Fig. 4(a) for $z \in [5, 10]\,\mu\mathrm{m}$ (solid line), differently from the case for $N_{\mathrm{D}} = 10^{14}\ \mathrm{cm}^{-3}$ (dashed line).

Detector performance is expected to worsen considerably in response to an increase of the detector donor doping, at least for what regards dark current. Infact, the latter is expected to increase, since Auger generation is no more suppressed by carrier depletion, as visible in Fig. 4(b): for $N_{\mathrm{D}} = 10^{14}\ \mathrm{cm}^{-3}$ (dashed line) the Auger generation is decreased by 1 order of magnitude in the absorber first three microns and by several order of magnitudes in the last two microns with respect to the case for $N_{\mathrm{D}} = 10^{15}\ \mathrm{cm}^{-3}$.

A possible remedy to compensate for the detrimental effect of higher N_D could be to consider a thinner absorber, i.e. the variant B. In Fig. 5 the electric field (panel (a)), and SRH and Auger generation rates (panel (b)) are plotted, calculated in the same calculation conditions (dark, $T = 140\,\mathrm{K}$, and $V_{\mathrm{bias}} = -0.5\,\mathrm{V}$) as for the case with the thickest absorber (variant A). However, comparing Fig. 4 and Fig. 5, we can see that the carrier depletion effect disappears as soon as N_D increases by 1 order of magnitude, no matter which variant (A or B) we are considering.

In summary, although very challenging values of absorber residual doping seem unavoidable in order to efficiently exploit the Auger suppression effects, a reduction of absorber thickness (variant B) is helpful to curtail the dark current. Fig. 6(a) shows the dark current density $J_{\mathrm{dark}} = I_{\mathrm{dark}}/a$ (where $a = 5\,\mu\mathrm{m}\times 5\,\mu\mathrm{m}$ is the pixel area) for variants A and B, and their shape is consistent with remarks made about Figs. 2–5: for the lowest value of N_D, when V_{bias} increases from zero to $-0.5\mathrm{V}$ the dark current density increases to a maximum value around 20 mV, then it progressively decreases for increasing reverse bias, confirming a behavior observed by other groups [8, 21] and caused by the progressive absorber carrier depletion. However, it is worth noting that, when N_D increases to $10^{15}\,\mathrm{cm}^{-3}$, this behavior almost disappears, irrespective of which variant is considered: carrier depletion becomes a marginal effect, and J_{dark} saturates to a value 2 orders of

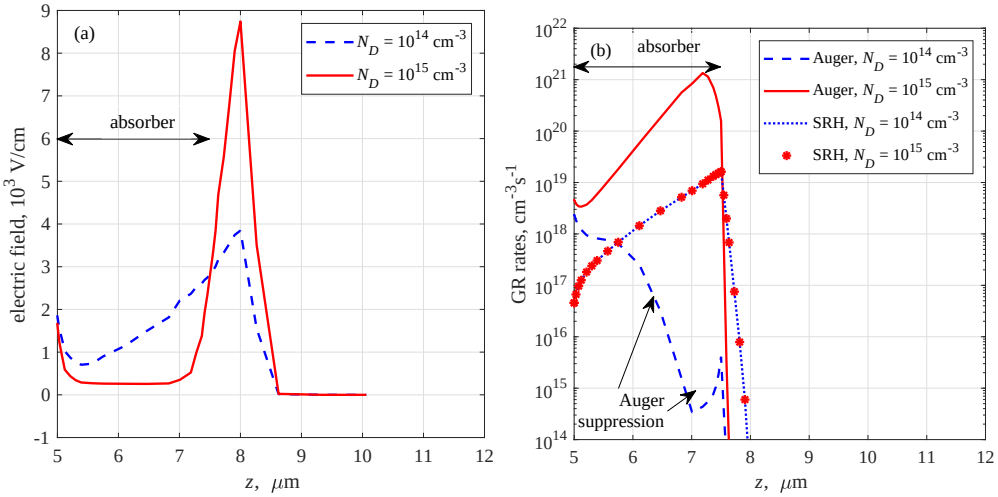

Fig. 5. Same quantities shown in Fig. 4, but for the variant B. Also in this case, for $N_{\rm D} = 10^{14}$ cm^{-3}, the suppression of Auger generation is well evident, disappearing for $N_{\rm D} = 1 \times 10^{15}$ cm^{-3}. The low bandgap absorber lies in $5 \le z \le 7.5$.

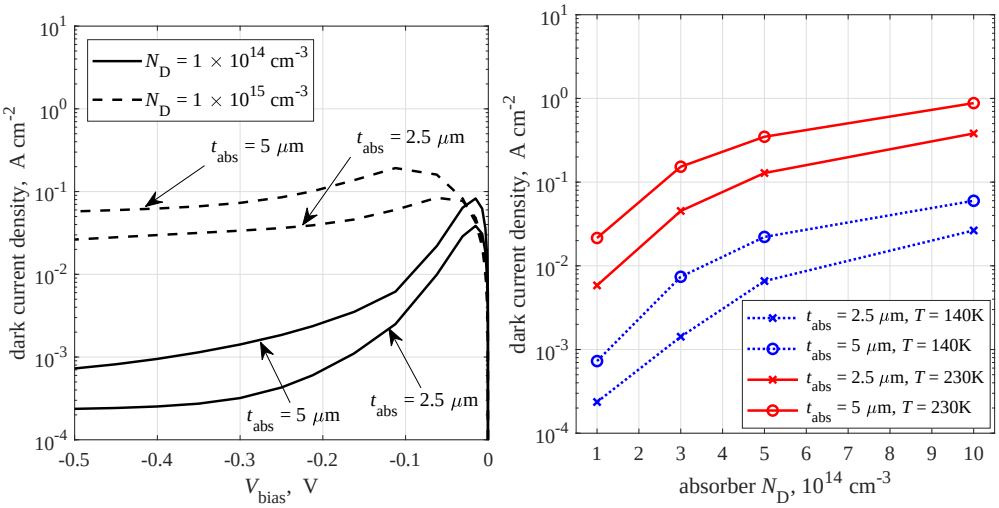

Fig. 6. (a) Dark current density for $T = 140$ K, $N_{\rm D} = 10^{14}$ cm^{-3} and $N_{\rm D} = 10^{15}$ cm^{-3}, for the two considered variants of $t_{\rm abs}$. (b) Comparison among dark current density at $V_{\rm bias} = -0.5$ V, for several values of $N_{\rm D}$, and for both variants A ($t_{\rm abs} = 5\,\mu$m) and B ($t_{\rm abs} = 2.5\,\mu$m).

magnitude higher.

In order to characterize the temperature behavior of this kind of detectors, we repeated the simulations in dark for $T = 180$ K and $T = 230$ K, the latter a much less demanding temperature in terms of cooling equipement characteristics. In order to compare the combined effects of temperature, N_D doping, and absorber thickness, Fig. 6(b) reports the value of the dark current density at $V_{\rm bias} = -0.5$ V, for several values of N_D in the considered interval, for the two extreme cases $T = 140$ K and 230 K, and considering both variants A and B. The most prominent variation of $J_{\rm dark}$ is against N_D and T: when N_D increases by 1 order of magnitude, $J_{\rm dark}$ increases by 2

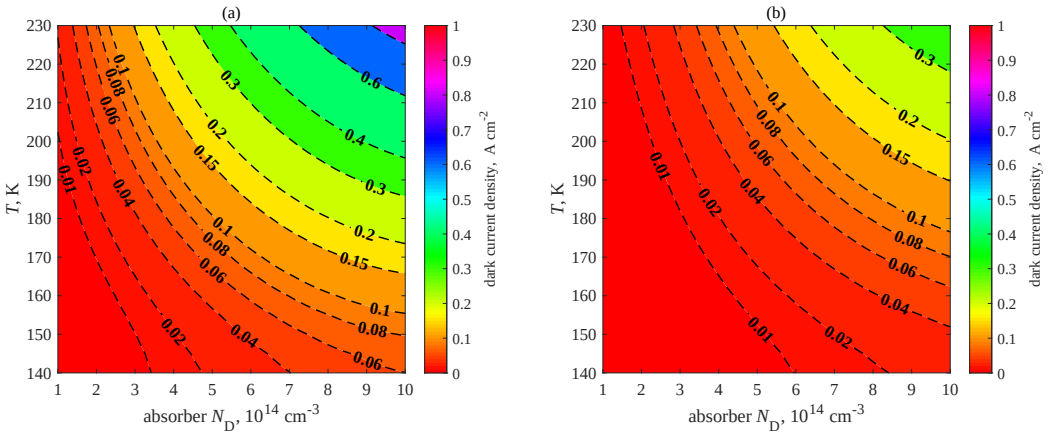

Fig. 7. The dark current density for $V_{\text{bias}} = -0.5$ V, as function of T and N_D, for variant A (a) and variant B (b).

orders of magnitude when $T = 140$ K, and a little less when $T = 230$ K, for both variants A and B. The considered increase of T makes J_{dark} to increase by 1 order of magnitude for all values of N_D and t_{abs}. Instead, the variation of dark current with t_{abs} is smaller: halving the absorber, J_{dark} decreases approximately by a factor between 2 and 3, depending on N_D and T.

Starting from these results, it is possible to find e.g. which pairs (N_D, T) provide the same dark current density, as done in Fig. 7, for both absorber thickness variants A and B. The figure (and similar ones, obtained further extending the variation domain) may be employed, for example, to find what is the temperature decrease required to obtain the same dark current with a higher doping. The figure can be useful when it is necessary to look for compromises, in case very-low-doping requirements are too difficult to fulfill.

4.2. *Simulations under illumination*

Aiming at assessing the electro-optic combined effects of N_D, T, and t_{abs}, electromagnetic (FDTD) and electrical (FB, drift-diffusion) simulations have been performed still considering $N_D \in [10^{14}, 10^{15}]$ cm^{-3}, $T \in [140, 230]$ K, for both absorber variants A and B, where the illumination is a monochromatic Gaussian beam with $\lambda = 5\,\mu$m, whose characteristics have been described in Section 2. Before discussing the simulation results in the considered parameters space, we can make some general remarks about the QE_{CP} spectrum, calculated according to Eq. 2 for the thickest absorber case and $N_D = 10^{14}$ cm^{-3} (one of the cases), considering $T = 140$ K and $T = 230$ K, and shown in Fig. 8(a). Defining the cutoff as the wavelength λ_c for which the QE_{CP} is half of its maximum, Fig. 8(a) indicates that $\lambda_c \approx 9\,\mu$m for $T = 140$ K, and it decreases to $\lambda_c \approx 7.5\,\mu$m for $T = 230$ K. Each spectrum consists of 84 λ-points, therefore it represents the result of 84 distincts electromagnetic and electrical simulations: the time needed to obtain each spectrum on our multi-core computational facilities is more than 40 hours, justifying the choice to perform the systematic simulation campaign across the parameter space just for a single wavelength. The choice $\lambda = 5\,\mu$m derives from the spectra shape in Fig. 8(a): it is a λ-value at the upper limit of the MWIR band, well below λ_c for both values of T.

The quantitative effect of T, N_D and t_{abs} on the diffusive inter-pixel crosstalk $\mathcal{D}_{\text{NNs}}$, the figure of merit that singles out the diffusion effects under illumination, can be seen in Fig. 8(b). The parameter that most efficiently acts on $\mathcal{D}_{\text{NNs}}$ is the absorber thickness: when halving t_{abs}, the crosstalk $\mathcal{D}_{\text{NNs}}$ approximately decreases by a factor of four. The behavior is reasonable, since the probability that photogenerated carriers are collected by the CP, before they diffuse laterally

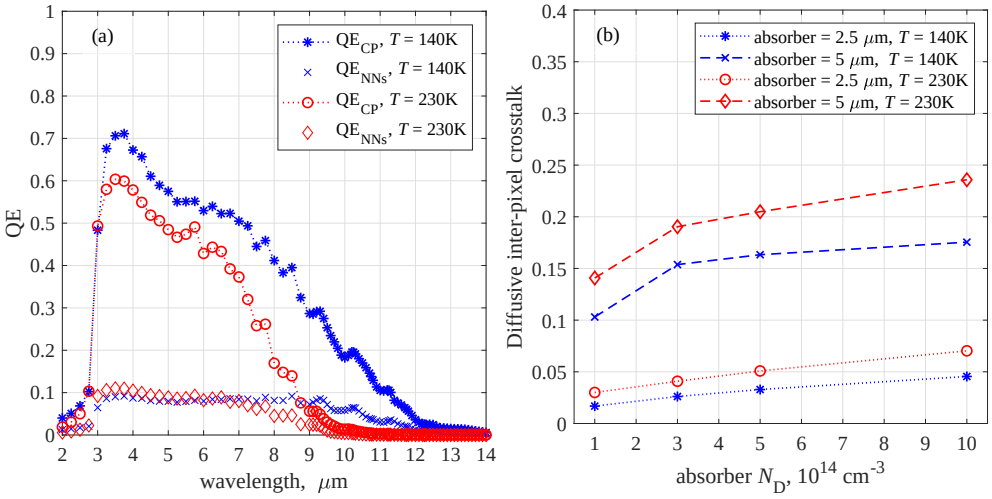

Fig. 8. (a) The CP and NNs spectral QE for the described Gaussian beam illumination centered on the CP for the variant A and $N_D = 10^{14}\,\mathrm{cm}^{-3}$, and (b) the diffusive inter-pixel crosstalk, simulated for the two considered variants A and B, for $T = 140\,\mathrm{K}$ and 230 K, with reverse bias polarization ($V_{\mathrm{bias}} = -0.5\,\mathrm{V}$).

towards the NNs, is supposed to increase when t_{abs} decreases, just for geometrical reasons, as pointed out and investigated in depth in Ref. [53].

A reduction of $\mathcal{D}_{\mathrm{NNs}}$ when N_D decreases by 1 order of magnitude is visible for both variants A and B (the variation is more substantial for the thicker absorber) and for all temperature values: when N_D decreases, the carrier depletion becomes more efficient (Fig. 3), and a not negligible electric field is present in a wider region of the absorber (see Fig. 4 and Fig. 5). Still in agreement with considerations in [53], when N_D decreases, carrier depletion and the resulting more extended electric field helps in sweeping out the photogenerated carriers before they diffuse laterally. Regarding the behavior of $\mathcal{D}_{\mathrm{NNs}}$ with T, Fig. 8(b) shows that, when increasing T, the crosstalk $\mathcal{D}_{\mathrm{NNs}}$ increases for all the considered values of N_D and t_{abs}, a behavior due to the reduction of $I_{ph,\,\mathrm{CP}}$, that increases a little the ratio $I_{ph,\,\mathrm{NNs}}/I_{ph,\,\mathrm{CP}}$, the dominant term in Eq. 5.

5. Conclusions

We simulated a HgCdTe-based MWIR planar 5×5 pixels FPA with 5 μm-wide square pixels, considering a small modification of a literature example, assessing the effect of the absorber doping, its thickness and the effect of temperature, both in dark and under illumination. It is found that, when T increases from 140K to 230K, the dark current increases 1 order of magnitude, whereas it decreases by 2 orders of magnitude in case N_D decreases from $10^{15}\,\mathrm{cm}^{-3}$ to $10^{14}\,\mathrm{cm}^{-3}$. In view of looking for trade-offs in case very-low-doping requirements are too difficult to fulfill, we assessed the effect of the absorber thickness, but when reducing t_{abs} from 5 μm to 2.5 μm the dark current decreases only by a factor of ≈ 3: the benefit is only moderate. The present simulations indicate that, at least for this class of detectors, the path towards room-temperature operation has quite stringent requirements on the residual doping.

Differently from the behavior in dark, under the considered Gaussian illumination the inter-pixel crosstalk is found to increase only moderately when the temperature and absorber residual doping increase in the considered intervals, whereas it can be reduced by more than a factor of three when the absorber thickness is halved.

6. Disclosures

Disclosures. The authors declare no conflicts of interest.

References

1. A. Rogalski, J. Antoszewski, and L. Faraone, "Third-generation infrared photodetector arrays," J. Appl. Phys. **105**, 091101 (2009).
2. P. Martyniuk, J. Antoszewski, M. Martyniuk, L. Faraone, and A. Rogalski, "New concepts in infrared photodetector designs," Appl. Phys. Rev. **1**, 041102 (2014).
3. O. Gravrand, J. Rothman, C. Cervera, N. Baier, C. Lobre, J. P. Zanatta, O. Boulade, V. Moreau, and B. Fieque, "HgCdTe detectors for space and science imaging: general issues and latest achievements," J. Electron. Mater. **45**, 4532–4541 (2016).
4. A. Rogalski, P. Martyniuk, and M. Kopytko, "Type-II superlattice photodetectors versus HgCdTe photodiodes," Prog. Quantum Electron. p. 100228 (2019).
5. R. K. Bhan and V. Dhar, "Recent infrared detector technologies, applications, trends and development of HgCdTe based cooled infrared focal plane arrays and their characterization," Opto-Electron. Rev. **27**, 174–193 (2019).
6. M. A. Kinch, "Fundamental physics of infrared detector materials," J. Electron. Mater. **29**, 809–817 (2000).
7. M. A. Kinch, "The future of infrared; III-Vs or HgCdTe?" J. Electron. Mater. **44**, 2969–2976 (2015).
8. J. Schuster, R. E. DeWames, and P. S. Wijewarnasurya, "Dark currents in a fully-depleted LWIR HgCdTe P-on-n heterojunction: analytical and numerical simulations," J. Electron. Mater. **46**, 6295–6305 (2017).
9. T. Ashley and C. T. Elliott, "Model for minority carrier lifetimes in doped HgCdTe," Electron. Lett. **21**, 451–452 (1985).
10. C. T. Elliott, "Non-equilibrium modes of operation of narrow-gap semiconductor devices," Semicond. Sci. Tech. **5**, S30 (1990).
11. P. Martyniuk and A. Rogalski, "HOT infrared photodetectors," Opto-Electron. Rev. **21**, 239–257 (2013).
12. P. Madejczyk, W. Gawron, P. Martyniuk, A. Keblowski, W. Pusz, J. Pawluczyk, M. Kopytko, J. Rutkowski, A. Rogalski, and J. Piotrowski, "Engineering steps for optimizing high temperature LWIR HgCdTe photodiodes," Infrared Phys. Tech. **81**, 276–281 (2017).
13. H. Lutz, R. Breiter, D. Eich, H. Figgemeier, and S. Hanna, "Improved high performance MCT MWIR and LWIR modules," in *Infrared Technology and Applications XLV,* vol. 11002, Proceedings of the SPIE (2019), p. 1100216.
14. P. Wang, H. Xia, Q. Li, F. Wang, L. Zhang, T. Li, P. Martyniuk, A. Rogalski, and W. Hu, "Sensing infrared photons at room temperature: from bulk materials to atomic layers," SMALL **15**, 1904396 (2019).
15. S. Maimon and G. W. Wicks, "*nBn* detector, an infrared detector with reduced dark current and higher operating temperature," Appl. Phys. Lett. **89**, 151109 (2006).
16. A. M. Itsuno, J. D. Phillips, and S. Velicu, "Predicted performance improvement of Auger-suppressed HgCdTe photodiodes and *p-n* heterojunction detectors," IEEE Trans. Electron Devices **58**, 501—507 (2011).
17. A. M. Itsuno, J. D. Phillips, and S. Velicu, "Mid-wave infrared HgCdTe nBn photodetector," Appl. Phys. Lett. **100**, 161102 (2012).
18. J. Schuster, W. E. Tennant, E. Bellotti, and P. S. Wijewarnasuriya, "Analysis of the Auger recombination rate in $P^+N^-n^-N^-N$ HgCdTe detectors for HOT applications," in *Infrared Technology and Applications XLII,* vol. 9819, Proceedings of the SPIE (2016), p. 98191F.
19. W. Lei, J. Antoszewski, and L. Faraone, "Progress, challenges, and opportunities for HgCdTe infrared materials and detectors," Appl. Phys. Rev. **2**, 041303 (2015).
20. P. Martyniuk, W. Gawron, J. Pawluczyk, A. Keblowski, P. Madejezyk, and A. Rogalski, "Dark current suppression in HOT LWIR HgCdTe heterostructures operating in non-equilibrium mode," J. Infrared Millim. Waves **34**, 385–390 (2015).
21. A. Rogalski, M. Kopytko, and P. Martyniuk, "Performance prediction of p-i-n HgCdTe long-wavelength infrared HOT photodiodes," Appl. Opt. **57**, D11–D18 (2018).
22. W. E. Tennant, D. Lee, M. Zandian, E. Piquette, and M. Carmody, "MBE HgCdTe technology: A very general solution to IR detection, described by "Rule 07", a very convenient heuristic," J. Electron. Mater. **37**, 1406–1410 (2008).
23. C. A. Keasler and E. Bellotti, "A numerical study of broadband absorbers for visible to infrared detectors," Appl. Phys. Lett. **99**, 091109 (2011).
24. J. Schuster, B. Pinkie, S. Tobin, C. Keasler, D. D'Orsogna, and E. Bellotti, "Numerical simulation of third-generation HgCdTe detector pixel arrays," IEEE J. Sel. Top. Quantum Electron. **19**, 800415 (2013).
25. A. Rogalski, P. Martyniuk, and M. Kopytko, "Challenges of small-pixel infrared detectors: a review," Rep. Prog. Phys. **79**, 046501 (2016).
26. D. Eich, W. Schirmacher, S. Hanna, K.-M. Mahlein, P. Fries, and H. Figgemeier, "Progress of MCT detector technology at AIM towards smaller pitch and lower dark current," J. Electron. Mater. **46**, 5448–5457 (2017).
27. G. C. Holst and R. G. Driggers, "Small detectors in infrared system design," Opt. Eng. **51**, 096401 (2012).
28. R. G. Driggers, R. Vollmerhausen, J. P. Reynolds, J. Fanning, and G. C. Holst, "Infrared detector size: how low should you go?" Opt. Eng. **51**, 063202 (2012).

29. M. Vallone, M. Goano, F. Bertazzi, G. Ghione, W. Schirmacher, S. Hanna, and H. Figgemeier, "Simulation of small-pitch HgCdTe photodetectors," J. Electron. Mater. **46**, 5458–5470 (2017).
30. H. Lutz, R. Breiter, D. Eich, H. Figgemeier, S. Hanna, R. Oelmaier, and J. Wendler, "Towards ultra-small pixel pitch cooled MW and LW IR-modules," in *Infrared Technology and Applications XLIV,* vol. 10624, Proceedings of the SPIE (2018), p. 106240B.
31. M. Vallone, M. Goano, F. Bertazzi, G. Ghione, A. Palmieri, S. Hanna, D. Eich, and H. Figgemeier, "Reducing inter-pixel crosstalk in HgCdTe detectors," Opt. Quantum Electron. **52**, 25 (2020).
32. A. Rogalski, *Infrared and Terahertz Detectors* (CRC Press, Boca Raton, FL, 2019), 3rd ed.
33. H. Kroemer, "Nobel Lecture: Quasielectric fields and band offsets: teaching electrons new tricks," Rev. Mod. Phys. **73**, 783–793 (2001).
34. M. Vallone, M. Mandurrino, M. Goano, F. Bertazzi, G. Ghione, W. Schirmacher, S. Hanna, and H. Figgemeier, "Numerical modeling of SRH and tunneling mechanisms in high-operating-temperature MWIR HgCdTe photodetectors," J. Electron. Mater. **44**, 3056–3063 (2015).
35. M. Mandurrino, G. Verzellesi, M. Goano, M. Vallone, F. Bertazzi, G. Ghione, M. Meneghini, G. Meneghesso, and E. Zanoni, "Trap-assisted tunneling in InGaN/GaN LEDs: experiments and physics-based simulation," in *14th International Conference on Numerical Simulation of Optoelectronic Devices (NUSOD 2014),* (Palma de Mallorca, Spain, 2014), pp. 13–14.
36. M. Mandurrino, M. Goano, M. Vallone, F. Bertazzi, G. Ghione, G. Verzellesi, M. Meneghini, G. Meneghesso, and E. Zanoni, "Semiclassical simulation of trap-assisted tunneling in GaN-based light-emitting diodes," J. Comp. Electron. **14**, 444–455 (2015).
37. M. Mandurrino, G. Verzellesi, M. Goano, M. Vallone, F. Bertazzi, G. Ghione, M. Meneghini, G. Meneghesso, and E. Zanoni, "Physics-based modeling and experimental implications of trap-assisted tunneling in InGaN/GaN light-emitting diodes," Phys. Status Solidi A **212**, 947–953 (2015).
38. A. Rogalski, *Infrared Detectors* (CRC Press, Boca Raton, FL, 2011), 2nd ed.
39. P. Capper and J. Garland, eds., *Mercury Cadmium Telluride. Growth, Properties and Applications* (John Wiley & Sons, Chichester, U.K., 2011).
40. Synopsys, Inc., Mountain View, CA, *Sentaurus Device User Guide. Version N-2017.09* (2017).
41. M. Born and E. Wolf, *Principles of Optics. Electromagnetic Theory of Propagation, Interference and Diffraction of Light* (Cambridge University Press, Cambridge, U.K., 1999), 7th ed.
42. C. Keasler and E. Bellotti, "Three-dimensional electromagnetic and electrical simulation of HgCdTe pixel arrays," J. Electron. Mater. **40**, 1795–1801 (2011).
43. J. Liang, W. Hu, Z. Ye, L. Liao, Z. Li, X. Chen, and W. Lu, "Improved performance of HgCdTe infrared detector focal plane arrays by modulating light field based on photonic crystal structure," J. Appl. Phys. **115**, 184504 (2014).
44. O. Akın and H.-V. Demir, "High-efficiency low-crosstalk dielectric metasurfaces of mid-wave infrared focal plane arrays," Appl. Phys. Lett. **110**, 143106 (2017).
45. M. Vallone, M. Goano, F. Bertazzi, G. Ghione, S. Hanna, D. Eich, and H. Figgemeier, "FDTD simulation of compositionally graded HgCdTe photodetectors," Infrared Phys. Tech. **97**, 203–209 (2019).
46. J.-P. Berenger, "A perfectly matched layer for the absorption of electromagnetic waves," J. Comp. Phys. **114**, 185–200 (1994).
47. D. Vasileska, S. M. Goodnick, and G. Klimeck, *Computational Electronics. Semiclassical and Quantum Device Modeling and Simulation* (CRC Press, Boca Raton, FL, 2010).
48. K. Yee, "Numerical solution of initial boundary value problems involving Maxwell's equations in isotropic media," IEEE Trans. Antennas Propag. **14**, 302–307 (1966).
49. M. Vallone, M. Goano, F. Bertazzi, G. Ghione, W. Schirmacher, S. Hanna, and H. Figgemeier, "Comparing FDTD and ray tracing models in the numerical simulation of HgCdTe LWIR photodetectors," J. Electron. Mater. **45**, 4524–4531 (2016).
50. M. Vallone, A. Palmieri, M. Calciati, F. Bertazzi, F. Cappelluti, G. Ghione, M. Goano, M. Bahl, E. Heller, R. Scarmozzino, S. Hanna, D. Eich, and H. Figgemeier, "Non-monochromatic 3D optical simulation of HgCdTe focal plane arrays," J. Electron. Mater. **47**, 5742–5751 (2018).
51. F. Bertazzi, M. Goano, G. Ghione, A. Tibaldi, P. Debernardi, and E. Bellotti, "Electron transport," in *Handbook of Optoelectronic Device Modeling and Simulation,* J. Piprek, ed. (CRC Press, Boca Raton, FL, 2017), chap. 2, pp. 35–80.
52. M. Kopytko, K. Jóźwikowski, P. Martyniuk, and A. Rogalski, "Photon recycling effect in small pixel p-i-n HgCdTe long wavelength infrared photodiodes," Infrared Phys. Tech. **97**, 38–42 (2019).
53. M. Vallone, M. Goano, F. Bertazzi, G. Ghione, S. Hanna, D. Eich, and H. Figgemeier, "Diffusive-probabilistic model for inter-pixel crosstalk in HgCdTe focal plane arrays," IEEE J. Electron Devices Soc. **6**, 664–673 (2018).